Supporting Information for

CO_2 fluxing and carbon assimilation by arc melts during magma-limestone interaction

Frances M. Deegan*, Manfredo Capriolo, Valentin R. Troll, Franz A. Weis, Sara Callegaro, Simone Colucci, Carmela Freda, Valeria Misiti, László E. Aradi, Henrik Skogby, Herman Darmawan, and Harri Geiger

*Corresponding author: Frances M. Deegan
Email: frances.deegan@geo.uu.se

This PDF file includes:

Supporting text

Methods

Magma–limestone interaction experiments

The magma–limestone interaction experiments analysed for volatiles in this study were conducted using a Max Voggenreiter GmbH end-loaded piston cylinder at the HP-HT laboratory of experimental volcanology and geophysics at Istituto Nazionale di Geofisica e Vulcanologia (INGV), Rome, Italy. The experiments were designed to simulate entrainment of limestone xenoliths in both anhydrous and hydrous Merapi basaltic-andesitic melt at mid-crustal conditions. Pressure of 0.5 GPa and temperature of 1200 °C were employed to replicate super-liquidus conditions for Merapi basaltic-andesitic magma at ca. 15 km depth beneath the volcano. The experiments were conducted with short runtimes, appropriate for the onset of limestone assimilation in magma (0 to 300 s). The compositions of starting materials are presented in **Table S-1** and representative compositions of the experimental glasses are presented in **Table S-2**. Further details regarding the starting materials and experimental procedure can be found in Deegan *et al.* (2010) and are summarized here.

Summary of the starting materials. A brief description of the experimental starting materials is provided below.

(i) A sample of Merapi basaltic-andesite rock powder (from the 1994 block-and-ash flow deposits) was fused at T = 1300°C and P = 1 atm in a rapid-quench furnace to produce the nominally anhydrous Merapi starting glass. The glass was subsequently analysed for its major element composition by Electron Probe Micro Analysis (EPMA) at INGV Rome and verified crystal-free. Note that EPMA chemical maps were recently acquired on several anhydrous experiments in order to illustrate the textures involved in limestone assimilation (see **Fig. 1 of the main text** and **Figs. S-1 to S-3 below**).

(ii) The same sample of Merapi basaltic-andesite rock powder was doped with ca. 2 wt.% ultra-pure H_2O and fused at T = 1200 °C and P = 0.2 GPa in an internally heated pressure vessel to produce the hydrous Merapi starting glass. The glass was analysed for its major element composition by EPMA at INGV Rome and verified crystal-free. It was additionally analysed for its water content by Karl Fischer titration at the University of Hannover, Germany (see Deegan *et al*., 2010). In this study, we conducted volatile analysis of hydrous experiments only.

(iii) A sample of limestone, sourced from a carbonate platform to the south of Merapi, at Parangtritis (Java, Indonesia). The composition of the limestone was determined by X-Ray Fluorescence (XRF). The rock sample was cut into small cubes of ca. 1 to 3 mm side length before being loaded into the capsules.

Experimental method. To prepare the experimental charges, platinum capsules with 3 mm outer diameter were annealed, loaded with the starting materials (ca. 40 mg pulverized glass and a ca. 10 mg clast of limestone per experiment) and welded shut. The charges were then encased in 19.1 mm diameter NaCl-borosilicate glass-crushable alumina-pyrophyllite assemblies. This type of assembly generates an oxidizing environment (fO_2 ≈ NNO+2), similar to that of arc magmas. The assemblies were loaded in the pressure vessel of the piston cylinder, pressurized at ambient temperature to 0.5 GPa, and heated at a rate of 200 °C per minute from ambient temperature to 1180°C and then at 20 °C per minute from 1180 to 1200°C. At this point, the experimental runs were allowed to proceed for short time intervals ranging from 0 to 300 s. Pressure was monitored and maintained constant

throughout the entire experiment duration. The experiments were terminated by shutting down the power source, which induced rapid, isobaric quenching at 2000 °C/min to the glass transition. Isobaric fast quenching is important for many types of experiments, but particularly for our experiments where the objective was to preserve melt compositions and textures that formed during magma–limestone interaction. At the end of the runs, the capsules were retrieved from the pressure vessel, checked for volatile loss by weighing, and mounted in low-volatile epoxy resin. The samples were then gently polished until the capsule was opened along its long axis and a flat sample surface was exposed.

Element maps of magma–limestone interaction experiments. Quantitative wavelength dispersive X-ray spectroscopy (WDS) element maps of anhydrous magma–limestone interaction experiments were carried out at INGV Rome, Italy. The polished epoxy mounts were carbon coated to avoid charge build-up during analysis. The maps were conducted using a JEOL-JXA8200 EPMA instrument equipped with five spectrometers under standard operating conditions of 15 kV accelerating voltage and 10 nA beam current. Pixel sizes ranged from 2 to 3 µm and a dwell time of 120 ms per pixel was used. Five elements were measured per analysis (Al, Ca, K, Na, and Si; Na and K were analysed first to reduce loss during analysis). The area of the maps ranged between 2.5 to 5.7 mm^2, with a resolution of either 850 × 650, 850 × 750, or 900 × 700 pixels. The analytical run time was ca. 24 hours in total. Further details of EPMA at INGV Rome, including typical analytical precision, can be found in Nazzari *et al.* (2019).

Volatile analysis of experimental products

Sample preparation for microspectroscopic analysis. In preparation for microspectroscopic analysis, the polished epoxy mounts were gently cleaned using high purity ethanol and a small amount of 1 µm diamond paste to remove any traces of former coatings (*e.g.*, carbon). For FTIR spectroscopy, the beam needs to be able to pass through the sample. Therefore, the samples had to be completely removed from their platinum capsules and thinned. We prized the platinum-encased samples from the epoxy mounts and then proceeded to carefully extract the glassy experimental products out of the capsules using a fine-point, dentistry-grade scaler. The experimental glasses were then fixed on a glass slide using thermoplastic resin and polished using various particle size-grades of Al_2O_3 grinding paper to create glass wafers. The thicknesses of the glass wafers ranged from 117 to 145 µm and were measured with a digital micrometer with an accuracy of ±2 µm. Note that the samples were thinned on the opposite side of the surfaces that were exposed on the epoxy mounts to preserve the surfaces previously documented by Scanning Electron Microscopy (SEM) in Deegan *et al.* (2010), which allowed us to link the new volatile data to the major element compositions of the glasses. Since the samples are just a few mm long and contain many vesicles and fractures, they were extremely fragile and difficult to physically manipulate. For this reason, some sample wafers were irreparably damaged. However, several samples were successfully polished to wafers with their original textural relationships intact. These samples were analysed using FTIR and confocal Raman microspectroscopy.

Fourier Transform Infrared (FTIR) spectroscopy. FTIR spectra in the range 800–5000 cm^{-1} were acquired on glassy samples at the Swedish Museum of Natural History, Stockholm, Sweden, following a similar approach to that employed by Weis *et al.* (2015, 2016). The glasses were analysed using a Bruker Hyperion 2000 microscope equipped with a Globar source, a KBr beamsplitter, and an MCT detector. Cracks, vesicles, and microcrystals in the glass were avoided by applying small apertures (100 to 200 µm) for masking during analysis. Analysis points were guided by optical microscopy images of the glass wafers and previously obtained SEM images at various magnifications. A reference spectrum was acquired on epoxy resin, to test for interferences from any traces of resin that may have intersected the beam path. The acquired spectra were baseline

corrected using a polynomial function and the individual bands were fitted with the software PeakFit (see **Fig. 2a of the main text**). For calculating volatile concentrations, we adopted a sample density of 2.5 g/cm^3. H_2O contents were calculated using the band at around 4500 cm^{-1} and an absorption coefficient of 0.67 L · mol^{-1} · cm^{-1} (see Dixon et al. 1995 and Shishkina et al. 2010). Molecular CO_2 contents were calculated using the band at around 2348 cm^{-1} and an absorption coefficient of 830 L · mol^{-1} · cm^{-1} (see Behrens et al. 2004). CO_3 contents were calculated using the band at around 1430 cm^{-1} and an absorption coefficient of 317 L · mol^{-1} · cm^{-1} (see Shishkina et al. 2010). Uncertainties on our volatile concentration results are based on uncertainties in sample thickness, density, and absorbance and are estimated at ± 10 %. Note that we analysed a doubly polished wafer of the starting glass for its H_2O content and replicated the previously obtained value for the glass, within error, as measured by Karl Fisher titration (see Deegan *et al.*, 2010). The FTIR data are presented in **Table S-3**.

Confocal Raman microspectroscopy. Confocal Raman microspectroscopy analysis of unexposed fluid inclusions in Ca-normal and Ca-rich glasses of the experimental samples was conducted at the Research and Industrial Relations Center of the Faculty of Science, Eötvös Loránd University of Budapest, Hungary, using a HORIBA Jobin Yvon LabRAM HR 800 Raman microspectrometer. The method employed is similar to that described in Deegan *et al.* (2022). All the analysed experimental samples contain abundant µm-sized bubbles (*i.e.* fluid inclusions). Larger bubbles of several hundred µm are frequent in the experimental products, but most of them are exposed, implying that they lost their volatile content during opening and polishing (*i.e.* sectioning) of the capsules. In this study, Raman analysis was carried out on µm-sized fluid inclusions beneath the surface of the glass wafers that were produced for FTIR analysis (**Fig. S-4**). The internal reflections of spherical surfaces were observed by focusing and defocusing the sample surface in reflected light, which allowed us to locate and screen unexposed fluid inclusions in the glass wafers.

Raman spot analyses were carried out below the sample surface (generally from 2 to 42 µm deep) to characterize the volatile content of the unexposed fluid inclusions. An OLYMPUS 100 × (N.A. = 0.9) objective was used to focus the laser on the analysed sites. We employed a frequency doubled Nd–YAG green laser with 532 nm excitation wavelength, displaying a power of 120 mW at the source and 23 mW on the sample surface for 100 % laser power. We used a laser power spanning from 0.1 to 100 % for the experiment #379-17, and a constant laser power of 100 % for all the other experiments. The Raman microspectrometer was calibrated before the measurements to the Rayleigh line at 0 cm^{-1}. Raman spectra acquisition was conducted at ambient temperature, in both single- and multi-window settings (from 1 to 11 windows) in a spectral range from 70 to 4200 cm^{-1}, with a spectral resolution of ca. 0.8 cm^{-1} above 3000 cm^{-1}. A 100 µm confocal hole, a 1800 grooves/mm optical grating, 2 accumulations, and a 30 s (in a few cases 60 and 90, and exceptionally up to 200 s) exposure time were employed for Raman analysis. The acquired spectra were baseline corrected and processed using the LabSpec 5 software (see **Fig. 2b of the main text**). The relative amounts of volatile species in the unexposed fluid inclusions were calculated using the integrated band areas of the acquired Raman spectra, after baseline correction, peak fitting, deconvolution, and conversion into a model (N = 89 out of 163 acquired Raman spectra).

In confocal Raman microspectroscopy, the detection limit exclusively depends on the Raman signal, thus universal detection limits are not available as measurements and samples cannot be standardized. However, the uncertainty on the calculated relative amounts of volatile species is estimated at ≤ 0.2 mol.% (Berkesi *et al.*, 2017). Residues from previous carbon coatings on the sample surfaces were additionally analysed using confocal Raman microspectroscopy in order to test for a potential contamination source. The very weak signal of the first order (main) Raman bands from the analysed residues of carbon coatings demonstrates that their contribution to the acquired Raman spectra is negligible. Similarly, the very weak signal of the Raman band from atmospheric N_2 (acquired at different depths in the host glass) demonstrates that its contribution to the acquired Raman spectra is also negligible.

Since confocal Raman microspectroscopy cannot discern between liquid H_2O from the fluid inclusions and molecular H_2O from the host glass, only H_2O dissolved in CO_2 can be quantified as exclusively derived from the fluid inclusions. The comparison between Raman spectra of the fluid inclusions, their rim, and their host glass indicate that additional H_2O may occur as liquid H_2O in thin films along fluid inclusion boundaries in at least some cases. However, the undetectability of these thin films of liquid H_2O in the fluid inclusions by optical microscopy suggests a H_2O content of ≤ 20 mol.% (Frezzotti *et al*., 2012). In the present study, the H_2O content of fluid inclusions was exclusively quantified as H_2O dissolved in CO_2, and thus corresponds to a minimum estimate.

Lastly, we detected a characteristic Raman band of carbonates at ca. 720 cm^{-1} Raman shift during analysis of fluid inclusions in Ca-rich glass, which indicates the local occurrence of carbonates. Carbonates may occur as micro- or nano-crystals dispersed in the Ca-rich glass or, more likely, gathered at the interface between fluid and glass, resulting from carbonation of the Ca-rich glass. The confocal Raman microspectroscopy data are presented in **Table S-4**.

Supplementary Tables

Table S-1 Composition of starting materials used in magma–limestone interaction experiments. See Deegan *et al.* (2010) for details regarding the analytical procedures used to generate the data.

	Average composition (EMP) of anhydrous glass[1]		Average composition (EMP) of hydrous glass[2]		Whole rock analysis (XRF) of limestone added[4]
		σ (10)[3]		σ (9)[3]	
wt%					
SiO_2	54.11	0.60	51.83	0.43	0.28
TiO_2	0.85	0.09	0.89	0.05	0.01
Al_2O_3	18.98	0.17	18.08	0.24	0.13
FeO	7.89	0.56	8.17	0.16	0.01
MnO	0.24	0.03	0.20	0.03	0.00
MgO	2.98	0.13	2.97	0.08	0.40
CaO	8.89	0.17	9.19	0.16	56.72
Na_2O	3.56	0.13	3.48	0.09	0.12
K_2O	2.05	0.10	2.05	0.03	0.00
P_2O_5	0.29	0.04	0.34	0.04	0.03
Total	99.85		97.20		57.70
H_2O	n.d.		2.23		0.15
CO_2	n.d.		n.d.		44.93

[1]Glass synthesized by fusing Merapi basaltic-andesite whole rock powder in a Pt capsule at 1300 °C, 1 atm, in air.

[2]The same glass as above, but uniformly hydrated at Universität Hannover (Germany) and measured for water content by Karl Fischer titration.

[3]1σ standard deviation; the number in parentheses represents the number of analyses for each sample.

[4]XRF analysis carried out at IFM-GEOMAR (Kiel, Germany).

Abbreviations: EMP = electron microprobe; n.d. = not determined; XRF = X-ray fluorescence.

Table S-2 Representative electron microprobe analyses of Ca-normal and Ca-rich glasses in magma–limestone interaction experiments. See Deegan *et al.* (2010) for details regarding the analytical procedures used to generate the data.

Exp. #	Ca-normal glass				Ca-rich glass			
	379-17 (runtime = 0 s, hydrous)	376-11 (runtime = 90 s, hydrous)	386-19 (runtime = 300 s, hydrous)	374-5 (runtime = 300 s, hydrous)	379-17 (runtime = 0 s, hydrous)	376-11 (runtime = 90 s, hydrous)	386-19 (runtime = 300 s, hydrous)	374-5 (runtime = 300 s, hydrous)
wt%								
SiO_2	51.97	51.62	52.28	50.83	34.11	27.72	34.90	38.08
TiO_2	0.74	0.81	0.77	0.89	0.45	0.49	0.56	0.58
Al_2O_3	17.94	18.21	18.50	18.70	12.27	10.32	12.23	13.93
FeO	6.89	6.42	6.30	6.23	5.35	4.85	5.38	5.48
MnO	0.17	0.10	0.10	0.20	0.11	0.18	0.13	0.14
MgO	2.89	2.82	2.66	2.73	2.41	2.18	2.30	2.26
CaO	9.13	8.88	9.75	8.83	31.16	34.34	31.08	27.39
SrO	0.09	0.10	0.08	0.10	0.03	0.08	0.08	0.07
Na_2O	3.94	4.54	3.66	4.48	1.35	1.33	1.75	2.22
K_2O	2.40	2.48	2.50	2.26	0.73	0.65	0.79	1.21
P_2O_5	0.32	0.28	0.30	0.27	0.22	0.16	0.24	0.22
Total[1]	96.48	96.26	96.90	95.52	88.19	82.30	89.44	91.56

[1]Analysis totals are low, potentially due to a combination of dissolved volatiles (mainly CO_2) and unavoidable micro-bubbles intersecting the analytical beam path.

Abbreviations: Exp. # = Experiment number.

Table S-3 Volatile data obtained by FTIR on experimental glasses.

Sample description	Sample thickness (µm)	H_2O (wt.%)	CO_2^{mol} (µg/g)	CO_3^{2-} (µg/g)	CO_2^{tot} (µg/g)
Experimental starting material					
Merapi hydrous glass	38	2	0	703	703
Merapi hydrous glass (repeat)	38	n.d.	0	491	491
Experiment 379-17, 0 s, hydrous					
379-17 trav1-1 (Ca-normal glass)	117	1.7	479	2103	2582
379-17 trav1-2	117	1.8	589	2034	2623
379-17 trav1-3	117	2.1	708	2067	2775
379-17 trav1-4	117	2.1	782	2166	2948
379-17 trav1-5a	117	2.0	611	2005	2616
379-17 trav1-5b	117	2.1	823	2018	2841
379-17 trav1-6	117	2.1	313	1946	2258
379-17 trav1-7	117	2.1	698	2079	2777
379-17 trav1-8	120	2.1	674	2038	2712
379-17 trav1-9	120	2.2	868	2161	3029
379-17 trav1-10	120	2.2	648	2171	2819
379-17 trav1-11 (Ca-normal glass)	120	2.2	780	2174	2954
379-17 trav1-12 (Ca-rich glass)	120	2.0	744	2291	3035
379-17 trav1-13 (Ca-rich glass)	120	2.1	872	2187	3058
Experiment 386-19, 300 s, hydrous					
386-19 trav1-1 (Ca-rich glass)	143	1.4	0	3100*	3100*
386-19 trav1-2 (Ca-rich glass)	143	1.5	0	3100*	3100*
386-19 trav1-3 (Ca-rich glass)	143	0.8	0	3100*	3100*
386-19 trav2-1 (Ca-normal glass)	145	2.0	326	1775	2101
386-19 trav2-2 (Ca-normal glass)	145	2.2	669	1788	2457
386-19 trav2-3 (Ca-normal glass)	145	2.0	605	1810	2415
386-19 trav2-4 (Ca-normal glass)	145	2.0	617	1813	2430
386-19 trav2-5 (Ca-normal glass)	145	2.0	585	1908	2493
386-19 trav2-6 (Ca-normal glass)	145	1.9	259	3092	3351
386-19 trav2-7 (Ca-rich glass)	145	1.3	0	3100*	3100*
386-19 trav2-8 (Ca-rich glass)	145	0.9	0	3100*	3100*
386-19 trav2-9 (Ca-rich glass)	145	1.0	0	3100*	3100*
386-19 trav2-10 (Ca-rich glass)	145	1.2	0	3100*	3100*
386-19 trav2-11 (Ca-rich glass)	145	1.7	0	2933	2933
386-19 trav2-12 (Ca-normal glass)	145	1.9	643	1994	2637
386-19 trav2-13 (Ca-normal glass)	145	2.1	502	1779	2281
386-19 trav3-1 (Ca-normal glass)	140	2.2	271	1754	2025
386-19 trav3-2 (Ca-normal glass)	140	2.2	380	1815	2195
386-19 trav3-3 (Ca-normal glass)	140	2.2	590	1815	2405
386-19 trav3-4 (Ca-normal glass)	140	2.2	421	1838	2258
386-19 trav3-5 (Ca-normal glass)	140	1.6	843	1750	2594

Footnotes for Table S-3 (previous page):

*Indicates that the value is a minimum estimate (the CO_3^{2-} content in these cases could not be quantified because the CO_3^{2-} peaks were off-scale due to excessive absorption).

All data were obtained by Fourier Transform Infrared spectroscopy at the Swedish Museum of Natural History, Stockholm, Sweden. See text for detailed method description.

Abbreviations: CO_2^{mol} = molecular CO_2; CO_2^{tot} = total CO_2; n.d. = not determined.

Table S-4 Volatile species data obtained by confocal Raman microspectroscopy in unexposed fluid inclusions in experimental glasses.

Sample description			Volatile species proportions in fluid inclusions (in mol. %)							
Exp. #	Glass	Site	CO_2	CH_4	N_2	H_2S	CO	C_2H_6	H_2	H_2O
379-17	Ca-norm	Bubble 1	62.83	3.98	9.47	0.00	18.19	0.000	1.50	4.03
379-17	Ca-norm	Bubble 2	71.88	3.34	9.72	0.00	13.67	0.000	1.39	0.00
379-17	Ca-norm	Bubble 3*	75.87	2.84	9.06	0.00	12.23	0.000	n.d.	n.d.
379-17	Ca-norm	Bubble 4*	100.00	n.d.	n.d.	n.d.	n.d.	n.d.	n.d.	n.d.
379-17	Ca-norm	Bubble 5	65.96	2.23	11.05	0.00	19.53	0.000	1.23	0.00
379-17	Ca-norm	Bubble 6*	74.20	2.02	10.97	0.00	12.81	0.000	n.d.	0.00
379-17	Ca-norm	Bubble 7*	73.58	1.79	10.22	0.00	14.41	0.000	n.d.	0.00
379-17	Ca-norm	Bubble 8*	100.00	n.d.	n.d.	n.d.	n.d.	n.d.	n.d.	n.d.
379-17	Ca-norm	Bubble 9*	100.00	n.d.	n.d.	n.d.	n.d.	n.d.	n.d.	n.d.
379-17	Ca-rich	Bubble 10*	100.00	n.d.	n.d.	n.d.	n.d.	n.d.	n.d.	n.d.
379-17	Ca-rich	Bubble 11*	100.00	n.d.	n.d.	n.d.	n.d.	n.d.	n.d.	n.d.
379-17	Ca-rich	Bubble 12	80.28	0.00	12.41	0.00	7.31	0.000	0.00	0.00
376-11	Ca-norm	Bubble 1	65.90	0.22	19.25	0.05	11.13	0.000	2.12	1.32
376-11	Ca-norm	Bubble 2	93.34	0.00	1.36	0.03	3.47	0.000	0.26	1.55
376-11	Ca-norm	Bubble 3	94.22	0.00	0.80	0.01	3.33	0.000	0.00	1.64
376-11	Ca-rich	Bubble 4	97.16	0.00	0.00	0.00	1.33	0.000	0.00	1.51
376-11	Ca-rich	Bubble 5	97.43	0.00	0.00	0.00	0.96	0.000	0.00	1.62
375-7	Ca-norm	Bubble 1	71.24	0.98	5.78	0.10	17.87	0.000	3.19	0.84
375-7	Ca-norm	Bubble 2	70.53	0.94	6.33	0.10	17.31	0.000	3.07	1.73
375-7	Ca-rich	Bubble 3	97.23	0.00	0.37	0.00	1.24	0.000	0.00	1.16
375-7	Ca-rich	Bubble 4	96.69	0.00	0.00	0.00	1.90	0.000	0.00	1.41
375-7	Ca-rich	Bubble 5	96.49	0.00	0.00	0.00	1.93	0.000	0.31	1.27
374-5	Ca-norm	Bubble 1	77.74	0.00	13.68	0.00	6.03	0.000	0.00	2.55
374-5	Ca-norm	Bubble 2	81.94	0.00	13.38	0.00	4.67	0.000	0.00	0.00
374-5	Ca-norm	Bubble 3	80.25	0.11	9.46	0.00	7.82	0.005	1.22	1.14
374-5	Ca-norm	Bubble 4	76.85	0.00	5.59	0.00	7.65	0.000	6.61	3.31
374-5	Ca-rich	Bubble 5	96.92	0.00	0.00	0.00	1.68	0.000	0.00	1.39
374-5	Ca-rich	Bubble 6	96.08	0.00	0.00	0.00	2.48	0.000	0.38	1.06

*Indicates that the site was discarded from quantification of the volatile species abundance in fluid inclusions since some volatile species were not determined.

All data were obtained by confocal Raman microspectroscopy at the Research and Industrial Relations Center of the Faculty of Science, Eötvös Loránd University of Budapest, Hungary. Analytical details are provided in the Methods section above.

Abbreviations: Ca-norm = Ca-normal; n.d. = not determined.

Supplementary Figures

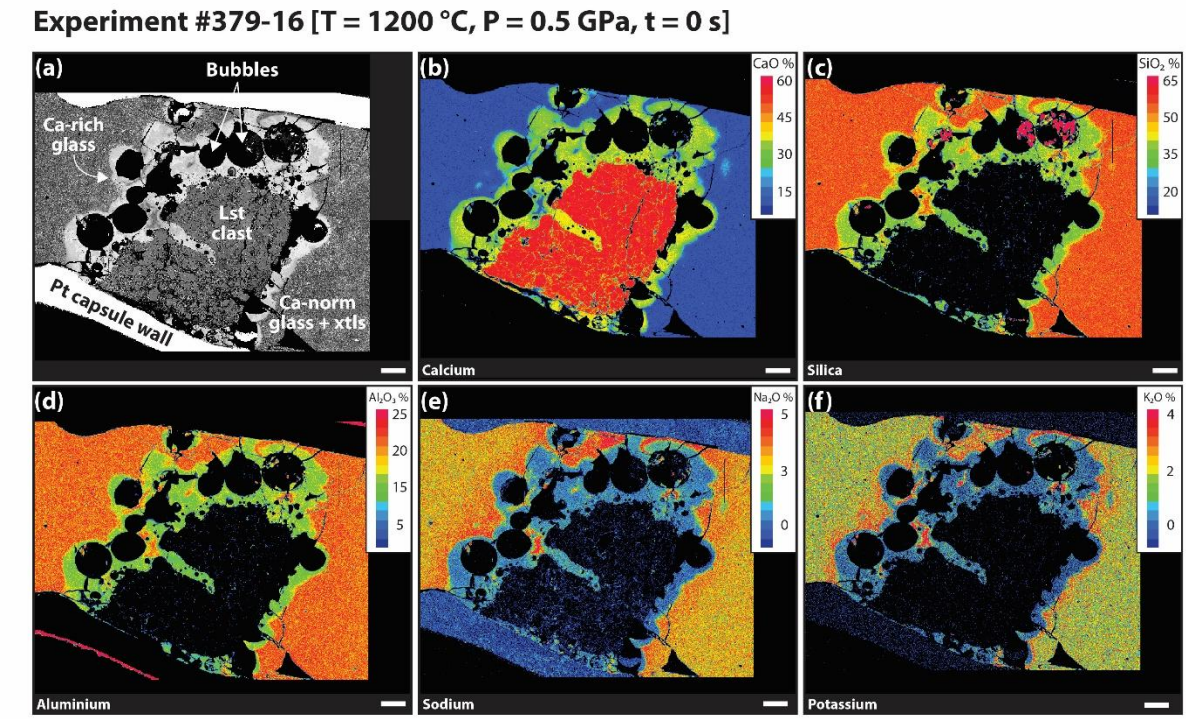

Figure S-1 (a) Back scattered electron image of a Merapi anhydrous magma–limestone interaction experiment with a runtime of 0 s. Calcium **(b)**, silica **(c)**, aluminium **(d)**, sodium **(e)**, and potassium **(f)** element maps of the same experiment. Limestone assimilation generates a Ca-rich silicate boundary layer (Ca-rich glass) in and around the limestone xenolith in addition to abundant fluid-filled bubbles. This experiment was first described in Deegan *et al.* (2010) and the element maps presented here were newly obtained for this study. Abbreviations: Ca-norm, Ca-normal glass; Lst, limestone; xtls, crystals. Scale bars = 200 µm.

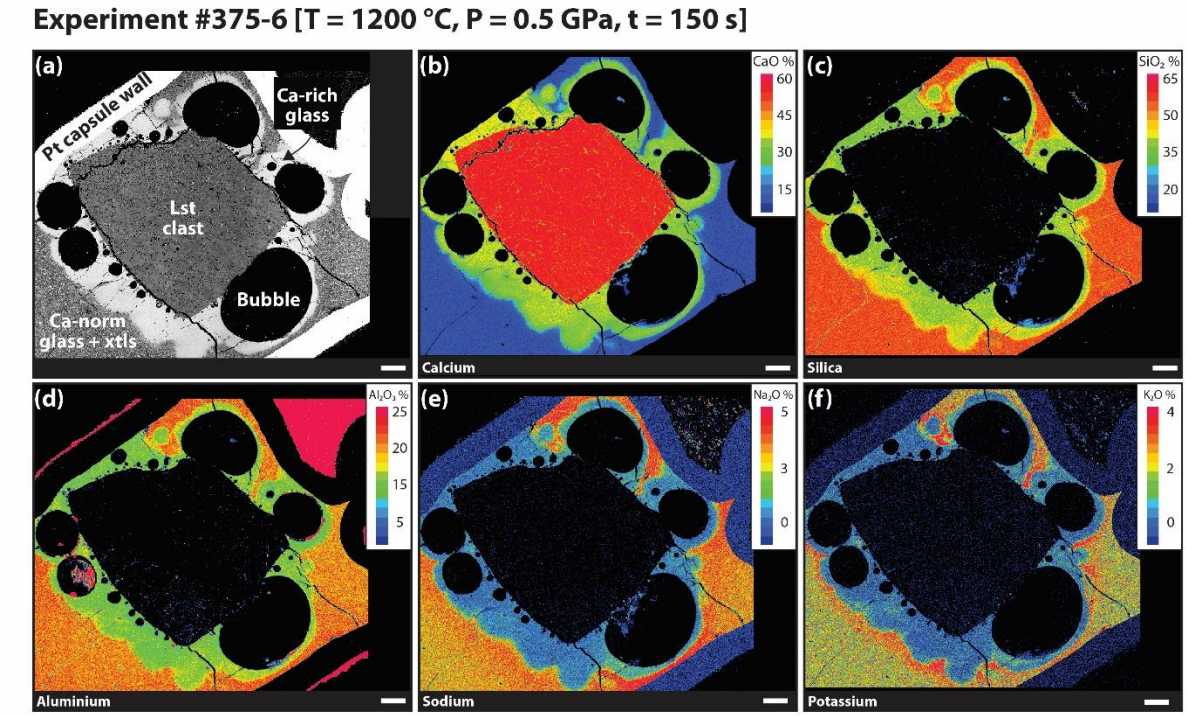

Figure S-2 (a) Back scattered electron image of a Merapi anhydrous magma–limestone interaction experiment with a runtime of 150 s. Calcium **(b)**, silica **(c)**, aluminium **(d)**, sodium **(e)**, and potassium **(f)** element maps of the same experiment. Limestone assimilation generates a CaO-rich silicate boundary layer (Ca-rich glass) around the limestone xenolith in addition to abundant fluid-filled bubbles. This experiment was first described in Deegan *et al.* (2010) and the element maps presented here were newly obtained for this study. Abbreviations: Ca-norm, Ca-normal glass; Lst, limestone; xtls, crystals. Scale bars = 200 µm.

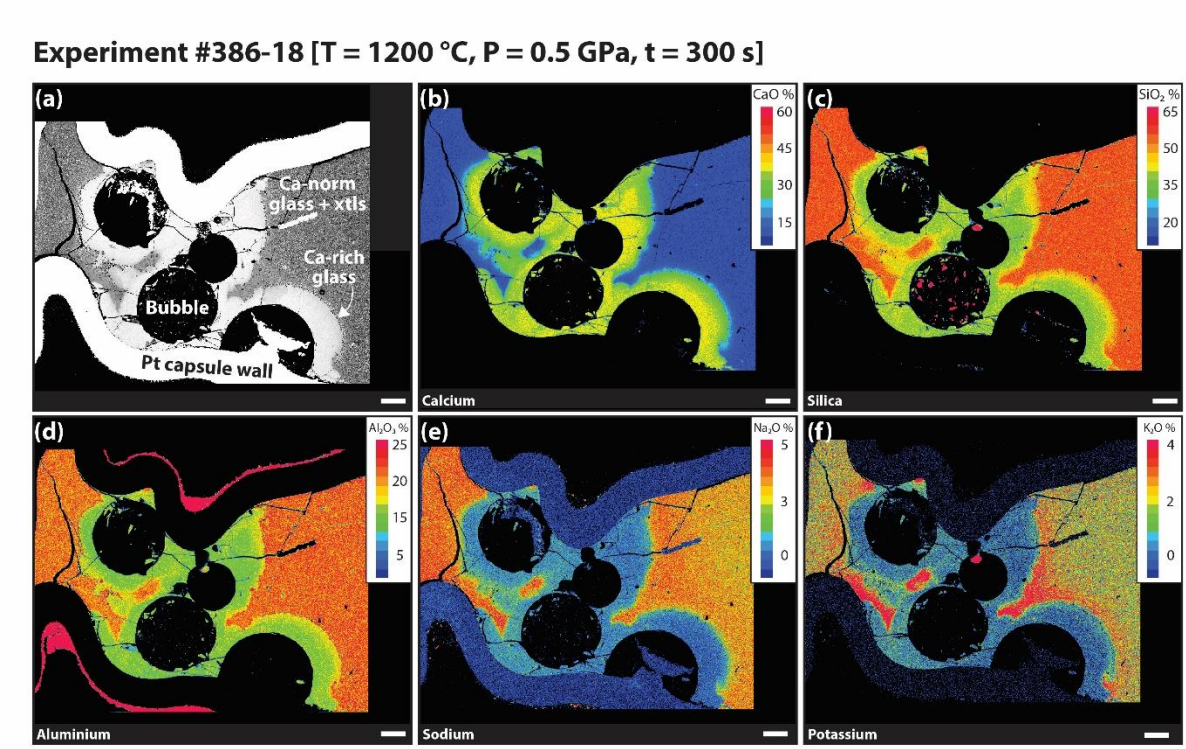

Figure S-3 (a) Back scattered electron image of a Merapi anhydrous magma–limestone interaction experiment with a runtime of 300 s. Calcium **(b)**, silica **(c)**, aluminium **(d)**, sodium **(e)**, and potassium **(f)** element maps of the same experiment. In this experiment, the limestone xenolith is completely assimilated into the melt, yielding a relatively large CaO-rich silicate boundary layer (Ca-rich glass) and abundant fluid-filled bubbles. This experiment was first described in Deegan *et al.* (2010) and the element maps presented here were newly obtained for this study. Abbreviations: Ca-norm, Ca-normal glass; xtls, crystals. Scale bars = 200 µm.

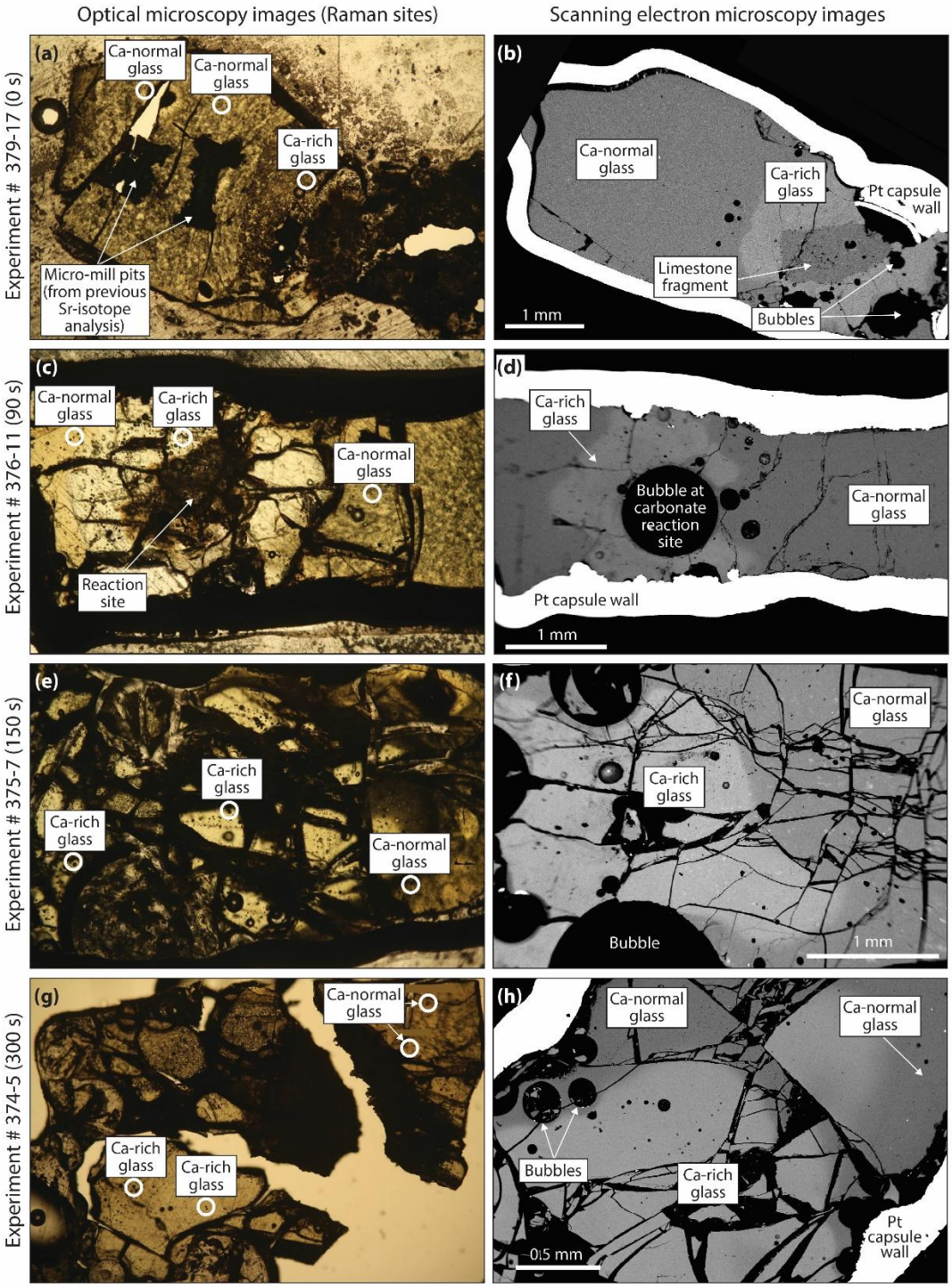

Figure S-4: (a, c, e, g) are optical microscopy images showing analysis sites for Raman microspectroscopy (white circles) of fluid inclusions in the products of four magma–limestone interaction experiments. **(b, d, f, h)** are corresponding Scanning Electron Microscopy (SEM) images showing detailed features of the experimental products (SEM images after Deegan *et al.*, 2010). Note that a remnant limestone fragment can be seen in the experiment with the shortest run time (panel b).

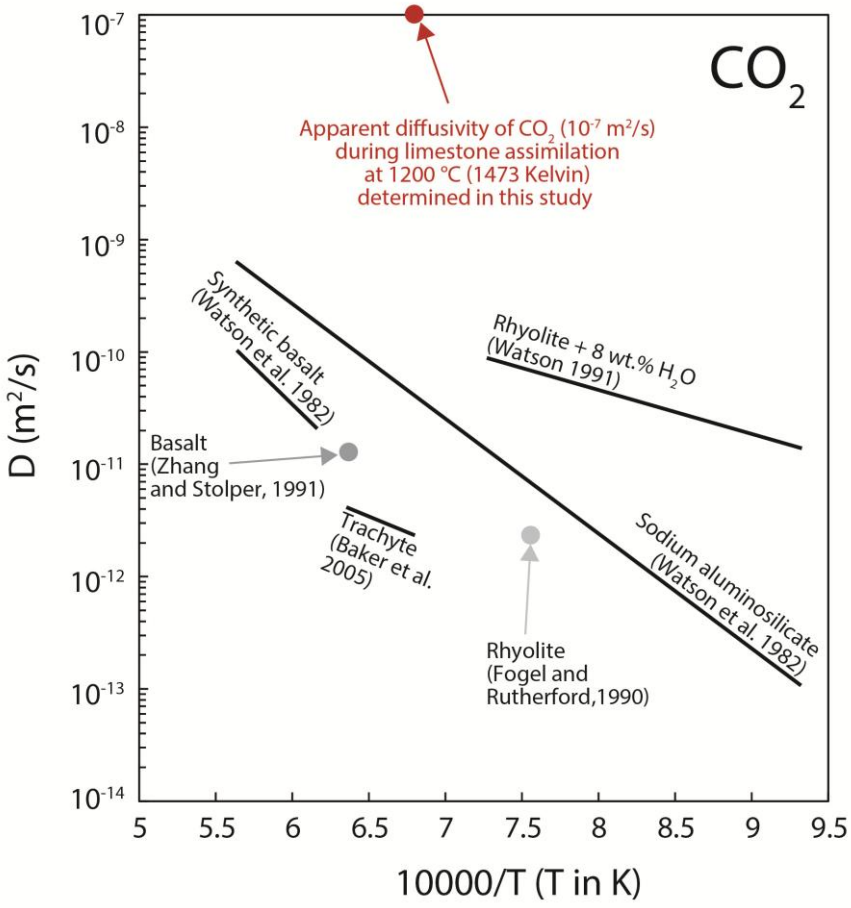

Figure S-5: Diffusivity of carbon dioxide in the limestone assimilation experiments of this study in comparison to various types of silicate melts. Figure modified after Baker et al. (2005).

SI References

Behrens, H., Ohlhorst, S., Holtz, F., Champenois, M. (2004) CO_2 solubility in dacitic melts equilibrated with H_2O-CO_2 fluids: Implications for modeling the solubility of CO_2 in silicic melts. *Geochimica et Cosmochimica Acta* 68, 4687-4703.

Berkesi, M., Káldos, R., Park, M., Szabó, C., Váczi, T., Török, K., Németh, B., Czuppon, G. (2017) Detection of small amounts of N_2 in CO_2-rich high-density fluid inclusions from mantle xenoliths. *European Journal of Mineralogy* 29, 423–431.

Deegan, F.M. *et al.* (2022) Magma–shale interaction in large igneous provinces: Implications for climate warming and sulfide genesis. *Journal of Petrology* 63, 1–10.

Deegan, F.M., Troll, V.R., Freda, C., Misiti, V., Chadwick, J.P., McLeod, C.L., Davidson, J.P. (2010) Magma-carbonate interaction processes and associated CO_2 release at Merapi volcano, Indonesia: Insights from experimental petrology. *Journal of Petrology* 51, 1027–1051.

Dixon, J.E., Stolper, E.M., Holloway, J.R. (1995) An experimental study of water and carbon dioxide solubilities in Mid-Ocean Ridge basaltic liquids. Part I: Calibration and solubility models. *Journal of Petrology* 36, 1607–1631.

Fogel, R.A., Rutherford, M.J. (1990) The solubility of carbon dioxide in rhyolitic melts: a quantitative FTIR study. *American Mineralogist* 75, 1311-1326.

Frezzotti, M.L., Tecce, F., Casagli, A. (2012) Raman spectroscopy for fluid inclusion analysis. *Journal of Geochemical Exploration* 112, 1–20.

Nazzari, M., Di Stefano, F., Mollo, S., Scarlato, P., Tecchiato, V., Ellis, B., Bachmann, O., Ferlito, C. (2019) Modeling the crystallization and emplacement conditions of a basaltic trachyandesitic sill at Mt. Etna volcano. *Minerals* 9, 126.

Shishkina, T., Botcharnikov, R.E., Holtz, F., Almeev, R.R., Portnyagin, M.V. (2010) Solubility of H_2O- and CO_2-bearing fluids in tholeiitic basalts at pressures up to 500 MPa. *Chemical Geology* 277, 115-125.

Watson, E.B. (1991) Diffusion of dissolved CO_2 and Cl in hydrous silicic to intermediate magmas. *Geochimica et Cosmochimica Acta* 55, 1897-1902.

Watson, E.B., Sneeringer, M.A., Ross, A. (1982) Diffusion of dissolved carbonate in magmas: experimental results and applications. *Earth and Planetary Science Letters* 61, 346-358.

Weis, F.A., Skogby, H., Troll, V.R., Deegan, F.M., Dahren, B. (2015) Magmatic water contents determined through clinopyroxene: Examples from the Western Canary Islands, Spain. *Geochemistry Geophysics Geosystems* 16, 2127–2146.

Weis, F.A., Stalder, R., Skogby, H. (2016) Experimental hydration of natural volcanic clinopyroxene phenocrysts under hydrothermal pressures (0.5-3 kbar). *American Mineralogist* 101, 2233–2247.

Zhang, Y., Stolper, E.M. (1991). Water diffusion in a basaltic melt. *Nature* 351, 306-309.